aerospace

MDPI

Article

Stealth Unmanned Aerial Vehicle Penetration Efficiency Optimization Based on Radar Detection Probability Model

Chengen Yuan, Dongli Ma, Yuhong Jia and Liang Zhang *

School of Aeronautical Science and Engineering, Beihang University, Beijing 100191, China; yuanchengen@buaa.edu.cn (C.Y.); madongli@buaa.edu.cn (D.M.); jiayuhong@buaa.edu.cn (Y.J.)
* Correspondence: microbeast@126.com

Abstract: Aerodynamic/stealth optimization is a key issue during the design of a stealth UAV. Balancing the weight of different incident angles of the RCS and combining stealth characteristics with aerodynamic characteristics are hotspots of aerodynamic/stealth optimization. To address this issue, this paper introduces a radar detection probability model to solve the weight balance problem of incident angles of the RCS and a penetration efficiency model to transfer the multi-object optimization into single-objective optimization. In this paper, a parameterized model of a flying-wing UAV is selected as the research object. A gradient-free optimization algorithm based on the genetic algorithm is used for maximizing efficiency. The optimization model balances the influence of the RCS mean value and RCS peak value on stealth performance. Moreover, the model achieves an optimal entire life cycle penetration efficiency coefficient by balancing aerodynamic and stealth optimization. The results show that the optimized model improves the penetration efficiency coefficient by 13.84% and increases maximum flight sorties by 1.8%. These results prove that the model has a reasonable combination of aerodynamic and stealth optimization for UAVs undertaking penetration missions.

Keywords: aerodynamic/stealth optimization; stealth unmanned aerial vehicle; radar detection probability; penetration efficiency; multidisciplinary optimization

check for updates

Citation: Yuan, C.; Ma, D.; Jia, Y.; Zhang, L. Stealth Unmanned Aerial Vehicle Penetration Efficiency Optimization Based on Radar Detection Probability Model. *Aerospace* **2024**, *11*, 561. https://doi.org/10.3390/aerospace11070561

Received: 31 May 2024
Revised: 5 July 2024
Accepted: 8 July 2024
Published: 9 July 2024

Copyright: © 2024 by the authors. Licensee MDPI, Basel, Switzerland. This article is an open access article distributed under the terms and conditions of the Creative Commons Attribution (CC BY) license (https://creativecommons.org/licenses/by/4.0/).

1. Introduction

Without achieving air supremacy, the survivability of combat aircraft is influenced by its radar stealth capabilities. Since the 1960s [1], radar cross-section (RCS) has been an important parameter for evaluating aircraft stealth ability. To enhance stealth performance while maintaining aerodynamic performance, engineers have focused on reducing right angle reflection and improving surface smoothness, as seen in fighters like the F-22 and bombers like the B-21. With the development and future application of combat UAVs, stealth performance is increasingly pivotal in aircraft design.

Aerodynamic efficiency is considered the most crucial aspect of the aircraft design phase. Optimization tailored to the requirements of a single discipline often leads to significantly different aircraft shapes depending on the optimization objective. Resolving this contradiction in the design process has become a research hotspot for aircraft engineers [2–4]. The F-117, the world's first stealth aircraft, served only 25 years despite its high combat survivability. Its sharp edges, which reduced its forward specular reflection and improved its stealth performance, significantly compromised its aerodynamic shape, resulting in a short cruise range. Its poor aerodynamic performance directly translated to reduced overall combat efficiency, contributing to its retirement. The retirement of the F-117 has greatly promoted comprehensive optimization efforts in aerodynamics and stealth. Typically, the approach involves using multi-objective optimization algorithms where the target objective combines cost functions with the lift-to-drag ratio and average RCS. By adjusting the weight factor of stealth optimization between these two objectives, the contradiction in the optimization process becomes apparent. Li et al. [5,6] demonstrated this by comparing their results with different weight factors. When all weight

factors prioritize stealth optimization, the lift–drag ratio decreased significantly from 26.04 to 16.94. Despite achieving excellent stealth performance, the optimized result proved unacceptable. This underscores how the choice of weight factors critically influences the optimization direction.

In some aerodynamic/stealth research, the Pareto optimal front is widely used for multidisciplinary optimization selection, combining the results from multi-objective optimization algorithms to select the desired outcomes. Wang et al. [7] initiated a flying-wing model with wingtips using a full factorial design and selected Pareto solutions to optimize both aerodynamic noise and RCS. Their research demonstrated the flexibility and comprehensiveness of Pareto solutions in analyzing multi-objective optimization results. Zia et al. [8] proposed a multidisciplinary design exploration and optimization framework to counter the issue of conflicting requirements of low drag and low RCS. By using the Computational Fluid Dynamics (CFD) and Shooting and Bouncing Rays (SBR) techniques, they developed a shared parameterized model for high-fidelity aerodynamic/stealth analysis. Additionally, they used a Gaussian Process (GP) surrogate model for efficiency and rapid assessment. The field of multi-objective optimization in aerodynamics continues to diversify and develop.

It is common to use the RCS mean value to represent stealth performance in optimization [9]. However, knowledge of an aircraft's RCS performance and radar parameters, such as the signal-to-noise ratio (SNR), reveals different radar detection distances at various incident angles. For example, radar typically detects an aircraft at a longer distance when incident waves are normal to the leading edge. This phenomenon, known as RCS peak exposure, is often masked by the RCS mean value assessment method. For instance, Ming Li's research [5] evaluated radar stealth characteristics using the RCS mean value over incident angles from -45° to $+45^\circ$ without considering the RCS peak value. Wu et al. [10] used the RCS mean value over angles from -90° to $+90^\circ$ to assess stealth performance. While widely used, these evaluation methods overlook the varying influence of incident wave angles and lack fidelity in assessing enemy detection during stealth aircraft penetration missions. In radar signal processing, Lu et al. [11] built a radar detection probability algorithm based on a statistical model of RCS dynamic fluctuations to analyze the effects of RCS peak exposure. However, Lu's focus was primarily on design and path planning methods to mitigate RCS peak effects rather than aircraft design itself. Li et al. [12,13] proposed a circumferential RCS scattering model to evaluate the stealth performance of penetration aircraft. This model introduces parameters for circumferential RCS features instead of relying solely on mean values, offering a new approach to assessing an aircraft's dynamic stealth performance. The existing research highlights the importance of distinguishing between RCS mean values and RCS peak values in aircraft stealth design. Developing a model that evaluates both mean values and peak exposures is crucial for improving the fidelity of RCS simulations.

Penetration assessment is considered one of the most important aspects of penetration path planning [14–16]. Some researchers [17,18] have proposed tactics for minimizing radar cross-sections to optimize path planning. They focus on designing effective methods to adjust flight attitudes and minimize the RCS exposed to radar, thereby reducing peak exposure. This underscores the necessity of minimizing the RCS peak value or altering its angle, which significantly influences flight path planning. Zhang's research [19] transformed the omnidirectional RCS of stealth UAVs into a detection probability function, revealing how different angles influence aircraft discovery. However, Zhang's research primarily focused on path planning rather than stealth UAV design. In contrast, Liu et al. [20] investigated a target detection probability model for penetration missions, which integrates the detection system, air defense system and aircraft RCS. While it enhances stealth aircraft probability fidelity, this model's complexity makes it less suitable for aerodynamic/stealth optimization. Moreover, this model has shortcomings, such as significantly increasing the computational load for ultra-high-fidelity probabilities.

This paper introduces a penetration efficiency model into an optimization framework to nonlinearly transform a multi-objective optimization model into a single-objective

optimization model. This assessment model integrates aerodynamics with stealth and decomposes the weighted problem of the RCS mean value and peak value through radar detection probability models. This paper presents a new idea and provides theoretical guidance for aerodynamic and stealth optimization of the design of future stealth UAVs.

2. Numerical Optimization Methodology

2.1. Geometric Parameterization

Lambda wings are a type of wing used in stealth UAVs, characterized by parallel leading and trailing edges. This feature ensures that the radar echo direction at the leading edge remains consistent with that of the trailing edge, enhancing stealth performance, which is beneficial for stealth penetration missions. Figure 1 shows the parametric geometry modeling, where b refers to the wing span, χ refers to the wing sweep angle, b_1 refers to the distance between the trailing edge turning point and wing root, φ refers to the wingtip twist angle and S refers to the wing area, which is fixed as 10.36 m^2. And C refers to chord length which is determined by the wing area, aspect ratio and wing sweep angle. In the subsequent discussion, b_1/b will be used to represent the position of the trailing edge turning point.

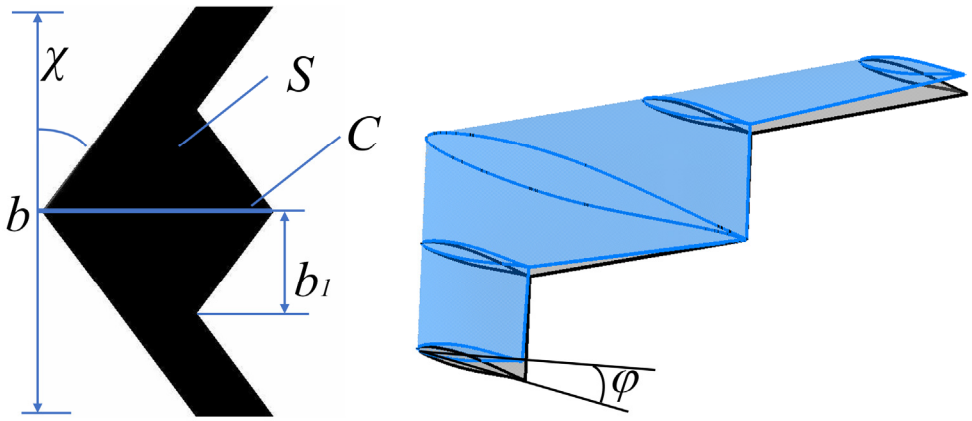


Figure 1. Parametric geometry modeling.

2.2. Numerical Solver

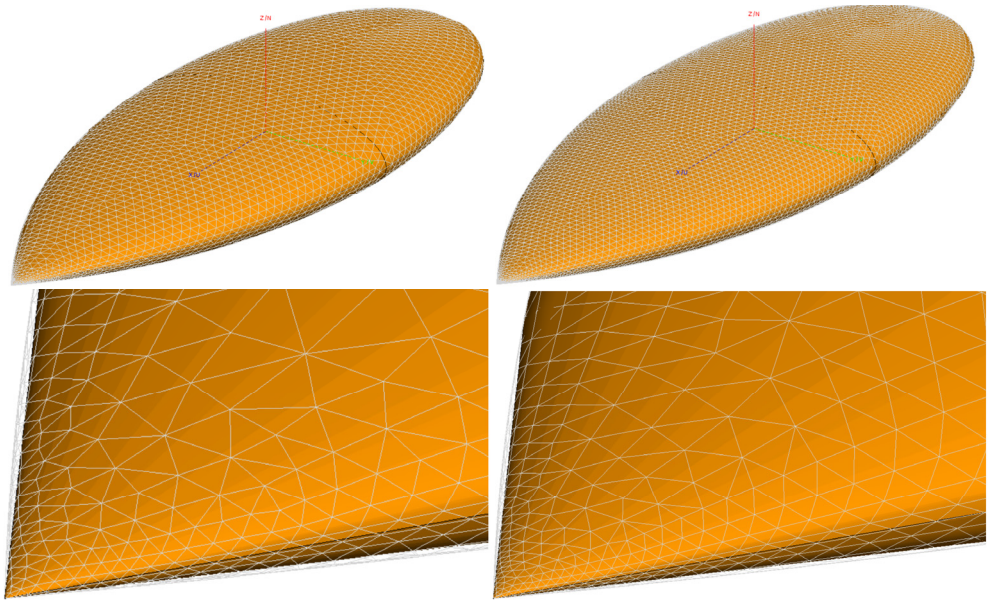
2.2.1. CEM Solver

The RCS characteristics depend on the configuration parameters, including wing shape and airfoil shape. This characteristic also depends on radar wave parameters such as frequency, SNR, gain and others. The accuracy and efficiency of the Computational Electromagnetics (CEM) solver are crucial to the fidelity of the entire optimization model. There are numerous CEM algorithms to calculate RCS, including multiple high-frequency approximate calculation methods based on Maxwell's equations, such as Geometric Optics (GO), Physical Optics (PO), the Geometric Diffraction Theory (GTD) and the Physical Theory of Diffraction (PTD) [21,22].

In this paper, the major computing domain is the smooth wing surface. Therefore, Physical Optics (PO), which offers a faster calculation speed and is more suitable for electrically large problems, smooth surfaces and weak coupling, is selected as the CEM algorithm method. Although Physical Optics cannot simulate edge diffraction effects and multiple bounce reflection effects, the method still provides high fidelity when the target object is a smooth surface.

To verify the computational accuracy of the CEM method, this paper utilizes the Almond test model from the Benchmark Radar Targets for the Validation of Computational Electromagnetic Programs proposed by NASA in 1993 for validation [23]. The benchmark model includes several smooth curved surfaces and a pointed top, consistent with the wing surface type. The consistency between the two models ensures the accuracy of the wing

under the CEM model. Figure 2 shows a mesh of the Almond at frequencies of 7 GHz and 9.92 Ghz. Figure 3 presents a comparison between the experimental and CEM results.



(**a**) f = 7 GHz (**b**) f = 9.92 GHz

Figure 2. NASA Almond mesh at f = 7 GHz and mesh at f = 9.92 GHz.

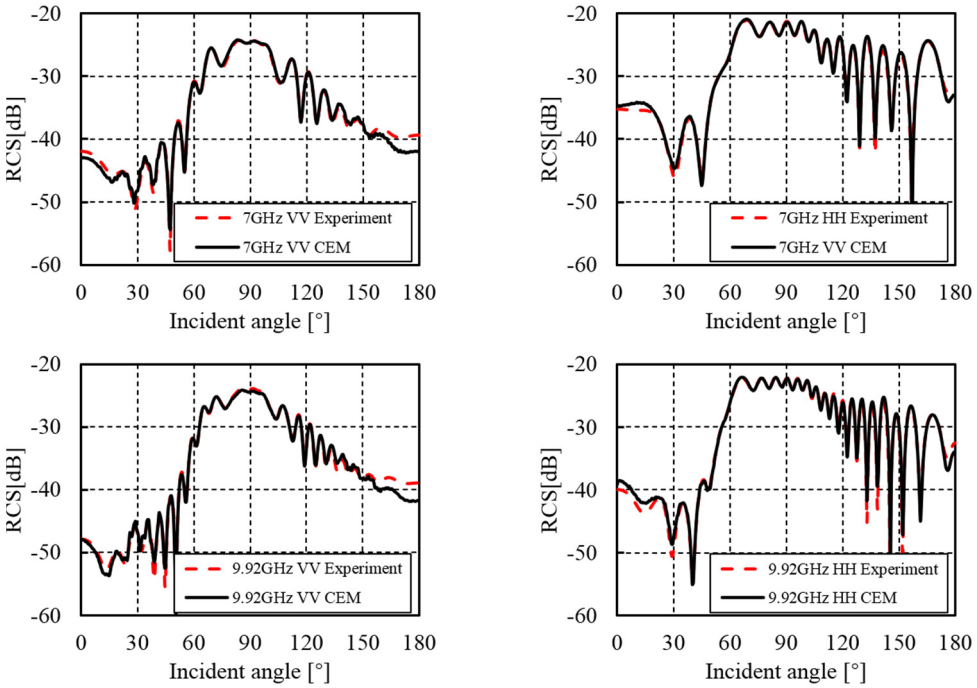


Figure 3. CEM results and experimental results under VV and HH polarizations.

According to the test results, the CEM method (based on PO) shows high accuracy for RCS simulation, especially for non-tip objects where the fit is extremely high. Considering that there are very few tips in the parameterized wing model, the PO CEM model is suitable for the optimization problem in this paper.

Vertical polarization and monostatic scattering are considered in this study. An unstructured surface mesh with the same density as the validation model is generated by the CEM solver. In the CEM computations, the radar parameters shown in Table 1 are referenced from the AN/SPY-1 radar [24].

Table 1. CEM parameters.

Radar Parameter	Value
Frequency	2 GHz (S)
Polarization	VV
SNR	30 dB
Pulse width	0.1 μs
Peak power	6.4 MW
Antenna gain	40 dB
Transmitter internal loss	1 dB
Receiver noise temperature	290 K
Scan rate (above horizon)	12 scan/min

2.2.2. CFD Solver

This paper uses the Reynolds-averaged Navier–Stokes (RANS) equation as the control equation and the shear stress transport (k-ω SST) turbulence model as the CFD method, verified by the DLR-F6-wing/body [25] model. The verified lift–drag curve is shown in Figure 4. Grids of DLF-R6 and the Lambda wing are shown in Figure 5. The control equations (RANS) are as follows:

$$\begin{gathered} \frac{\partial \rho}{\partial t} + \frac{\partial}{\partial x_i}(\rho u_i) = 0 \\ \frac{\partial}{\partial t}(\rho u_i) + \frac{\partial}{\partial x_i}(\rho u_j u_i) = -\frac{\partial p}{\partial x_i} + \frac{\partial \sigma_{ij}}{\partial x_j} + \frac{\partial}{\partial x_j}(-\rho u_i{}' u_j{}') \end{gathered} \tag{1}$$

And the turbulence model equations for the k-ω SST are as follows:

$$\begin{gathered} \frac{\partial k}{\partial t} + u_j \frac{\partial k}{\partial x_j} = \frac{1}{\rho} P_k \left(\frac{M_\infty}{\mathrm{Re}}\right) - \beta' k\omega \left(\frac{M_\infty}{\mathrm{Re}}\right) + \frac{1}{\rho}\frac{\partial}{\partial x_j}\left[\left(\mu + \frac{\mu_T}{\sigma_k}\right)\frac{\partial k}{\partial x_j}\right]\left(\frac{M_\infty}{\mathrm{Re}}\right) \\ \frac{\partial \omega}{\partial t} + u_j \frac{\partial \omega}{\partial x_j} = \frac{1}{\rho} P_\omega \left(\frac{M_\infty}{\mathrm{Re}}\right) - \beta \omega^2 \left(\frac{M_\infty}{\mathrm{Re}}\right) + \frac{1}{\rho}\frac{\partial}{\partial x_j}\left[\left(\mu + \frac{\mu_T}{\sigma_\omega}\right)\frac{\partial \omega}{\partial x_j}\right]\left(\frac{M_\infty}{\mathrm{Re}}\right) + 2(1-F_1)\sigma_{\omega 2}\frac{1}{\omega}\frac{\partial k}{\partial x_j}\frac{\partial \omega}{\partial x_j}\left(\frac{M_\infty}{\mathrm{Re}}\right) \end{gathered} \tag{2}$$

where ρ is the fluid density, $P_k P_\omega$ is the fluid pressure, $u_i u_j$ are the mean velocities, $u_i{}' u_j{}'$ is the Reynolds stress, k is the turbulence kinetic energy, μ is the dynamics viscosity, μ_T is the turbulent viscosity, σ_ω is the Prandtl number for frequency ω, σ_k is the Prandtl number for turbulence kinetic energy, σ_{ij} is the viscosity tensor, M_∞ is the fluid Mach number, Re is the Reynolds number, F_1 is the correction factor and $\beta\beta'$ are the default model coefficients.

Despite some fluctuation between these results and the experimental data, the verification results still demonstrate the feasibility of the numerical analysis methods. The aerodynamic computational states of the baseline geometry are summarized in Table 2.

Table 2. CFD parameters.

Flight State Parameter	Value
Static pressure	26,420 Pa
Mach number	0.65
Altitude	10 km
Density	0.412 kg/m^3
Temperature	223.15 K

This paper mainly studies the lift–drag and stealth characteristics of the Lambda wing during the cruise state. However, changes in configuration will also affect the UAVs' stability, maneuverability and handling characteristics, which will not be considered.

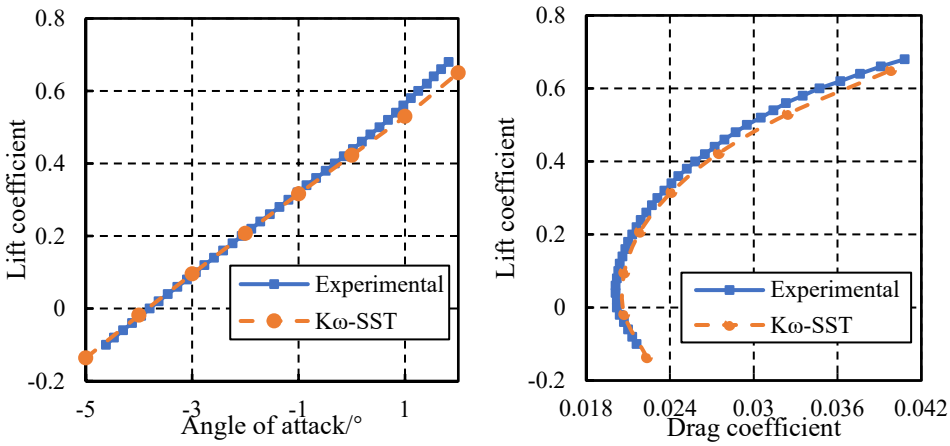


Figure 4. Numerical method compared with experimental method based on DLR-F6-Wing/Body model.

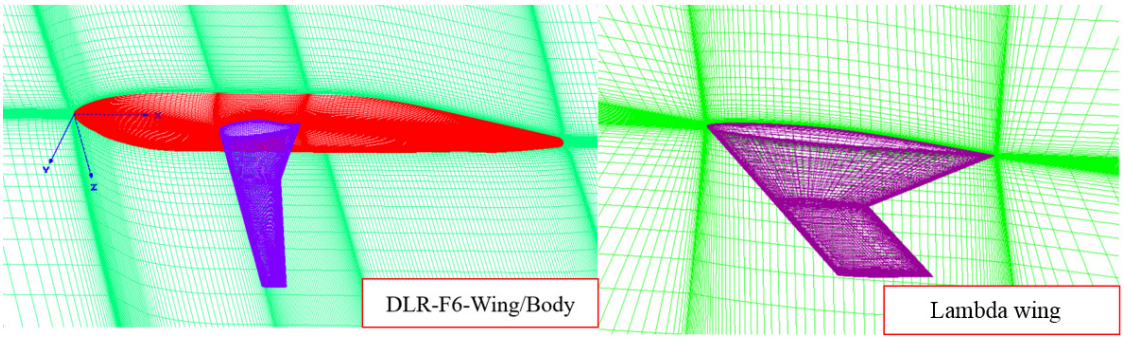


Figure 5. DLR-F6 grid and Lambda wing grid.

2.3. Aerodynamic/Stealth Optimization Methodology

First of all, this paper adopts a flying-wing parametric model with a single airfoil. The wing configuration is limited by several parameters other than the airfoil, which have a significant influence on the characteristics of lambda wings [26]. This chapter will first introduce the penetration efficiency model and present the optimization model of wing configuration.

2.3.1. Radar Detection Probability Model and Penetration Efficiency

During the airfoil optimization and wing configuration optimization, a 3D baseline wing is used to generate an RCS for the stealth part, and the detection probability is generated by the RCS, which is a part of the penetration efficiency model. The detection probability model simulates the process of aircraft arriving at enemy ground-combat targets and calculates the probability of aircraft being detected by enemy radar at unknown locations. Gaussian distribution-based models are widely used in simulations of unknown location [27] in various disciplines. In the battlefield, the closer to the combat target, the higher the probability of radar deployment, which is consistent with the Gaussian distribution. This paper selects a 2D Gaussian distribution to simulate the randomness of the radar position.

During the design stage, it is impossible to determine the position of enemy radar. Using as many radars as possible helps to improve the accuracy of radar detection probability. A total of 1×10^5 radars are scattered within a 1000 km range of penetration targets. And the covariance matrix of a two-dimensional Gaussian distribution is as follows:

$$\sigma = 1.11 \times 10^5 \begin{bmatrix} 1 & 0 \\ 0 & 1 \end{bmatrix} \tag{3}$$

$$G(x,y) = \frac{1}{2\pi\sigma^2} e^{-(x^2+y^2)/2\sigma^2} \tag{4}$$

where $G(x,y)$ refers to Gaussian distribution, (x,y) refers to the coordinates and σ refers to the covariance matrix.

The radar distribution is shown in Figure 6.

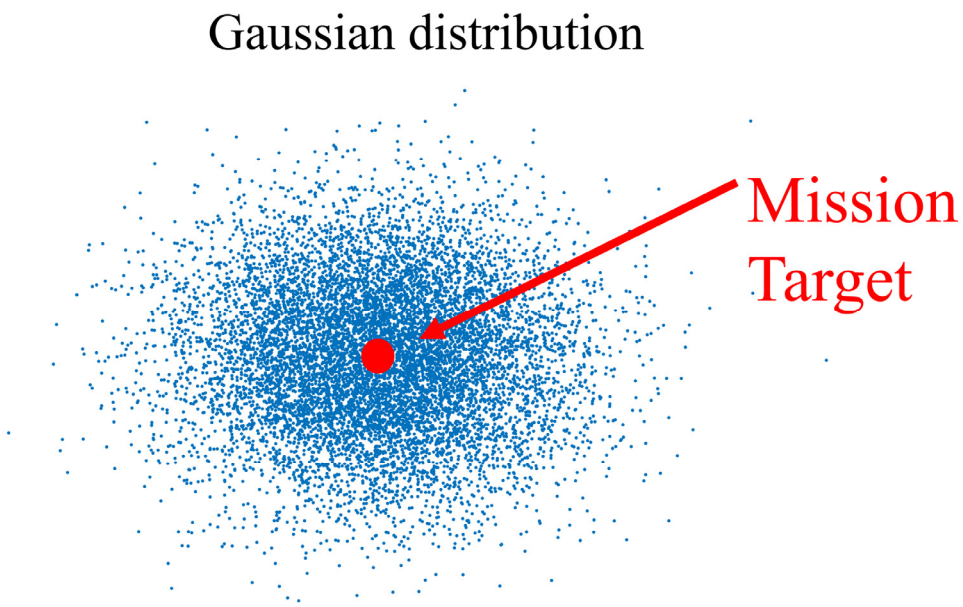


Figure 6. Radar position distribution using 2D Gaussian distribution.

The detection distance of an aircraft detected by radar is related to its RCS and to certain parameters of the radar itself. The radar range equation is as follows:

$$R_t{}^2 R_r{}^2 = \frac{\tau P_t G_t G_r \sigma_{\mathrm{RCS}} \lambda^2}{(4\pi)^3 (S/N)_{\min} k T_s L} \tag{5}$$

where the terms in the equation are defined as follows: P_t—peak transmit power in watts; G_t—transmitter gain; G_r—receiver gain; λ—radar operating frequency wavelength in meters; σ_{RCS}—target's nonfluctuating radar cross-section in square meters; L—general loss factor to account for both system and propagation loss; R_t—range from the transmitter to the target; R_r—range from the receiver to the target; τ—pulse duration; $(S/N)_{\min}$—signal-to-noise ratio; k—Boltzmann's constant; and T_s—receiver noise temperature.

This paper uses the AN/SPY-1 radar for simulation, which is a monostatic radar. This means that

$$R_t = R_r = R \tag{6}$$

and this equation degenerates into:

$$R = \left[\frac{\tau P_t G_t G_r \sigma_{\mathrm{RCS}} \lambda^2}{(4\pi)^3 (S/N)_{\min} k T_s L} \right]^{1/4} \tag{7}$$

where R is the detection range of the radar.

Conversely, if the radar parameters are determined, the RCS σ corresponds to the detection distance. Figure 7 shows that the conversion of the aircraft σ-Phi curve into an R-Phi curve. The left plot displays the relationship between the aircraft's forward RCS and incident angle, measured in [dBsm]. The right schematic illustrates the range where the aircraft can be detected after converting the RCS into the radar-detectable distance.

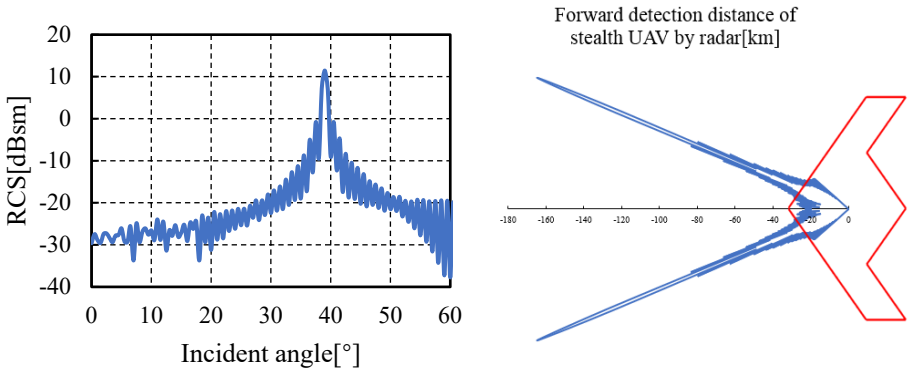


Figure 7. Transformation from RCS to detection range.

The flight altitude studied in this paper is 10 km, and the horizon distance calculated using the horizon calculation formula is 357 km. This distance is far greater than the radar detection range for the UAV. Therefore, it ensures the validity of the flat Earth model assumption, thereby guaranteeing the accuracy of the radar detection range equation. This makes the process of flying straight towards the target the worst scenario for survivability in the calculation model.

$$d_{horizon} = \sqrt{hD_{earth} + h^2} \tag{8}$$

In the above equation, $d_{horizon}$ is the horizon distance, h is the flight altitude and D_{earth} is the Earth' diameter.

When calculating the radar cross-section, focus is primarily on the forward direction of the aircraft due to the brief appearance of lateral radar wave crests, which are perpendicular to flight speed and complicate effective scanning. While optimizing wingtips is typically necessary for lateral stealth performance and often follows aerodynamic configuration optimization, this paper does not address wingtip optimization. Therefore, it calculates the RCS for incident angles within $\pm 60^\circ$ forward.

This paper uses the AN/SPY-1 radar as an example to calculate the radar detection probability. The parameters required for transforming the RCS to the radar detection distance are shown in Table 1.

To simplify the detection probability model, this paper considers radars falling within the range calculated by the radar distance equation capable of detecting the aircraft, while those falling outside this range are considered incapable of detecting the aircraft. During actual air combat, the radar system's lowest signal-to-noise ratio is adjustable or dynamic, leading to dynamic fluctuations in the radar detection range. Due to the large number of radar location samples, these SNR fluctuations are considered offset in the probability calculations. This paper assumes the enemy radar (AN/SPY-1) operates in a regular patrol mode with a scanning rate of 12 times per minute. Therefore, the radar detection speed is also related to the penetration speed. In this paper, the UAV's penetration speed is equal to its cruise speed.

$$D_r = t_s V_p \tag{9}$$

In the above equation, D_r is the detecting distance unit shown in Figure 8; t_s is the scan rate of the enemy radar; and V_p is the penetration speed of the UAV.

In real penetration scenarios, pulse Doppler radar requires multiple pulses to confirm the authenticity of the target. Otherwise, distinguishing between actual targets and environmental noise becomes challenging. Therefore, when calculating the radar detection probability, it is essential to exclude situations where the aircraft's exposure time on the radar is insufficient. Based on the high-fluctuation RCS characteristics of a stealth UAV with changes in incident angle, this paper uses a discrete scanning method to filter out parts of radars near peak positions. This method filters out radars near peak RCS positions, thereby simulating the influence of peak RCS values on radar detection probability models. A UAV that is scanned 4 times is considered the threshold for missile locking. Filtered

radars are shown in Figure 9: green dots represent radars too distant to detect, red dots represent radars that have fully captured the UAV and blue dots represent radars filtered out due to RCS peaks.

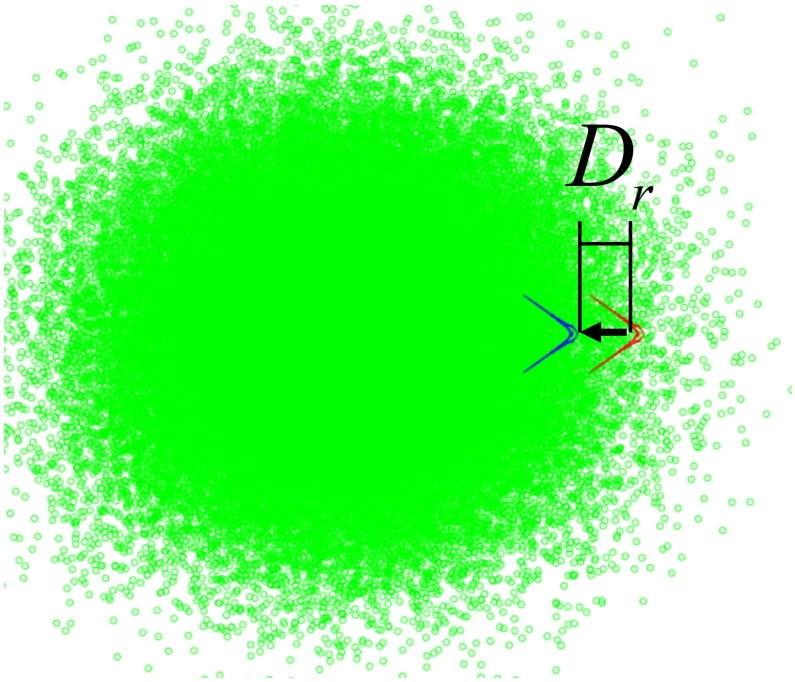


Figure 8. UAV flying over radar detection area.

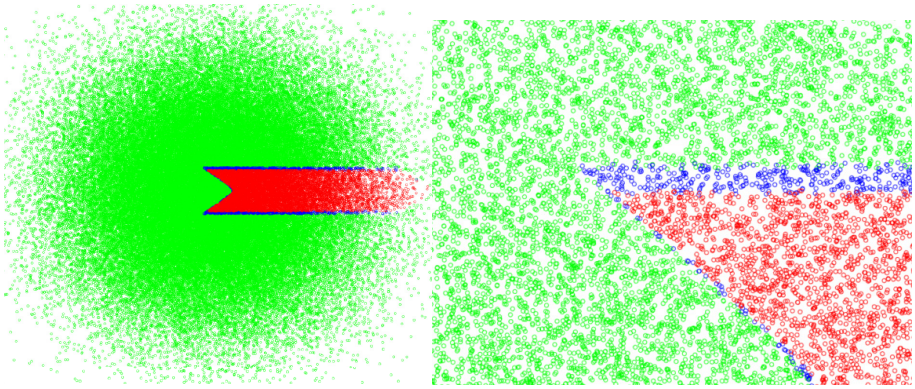


Figure 9. Radar detection and distribution during UAV penetration mission.

With movement from 1000 km away to the target position, all threat radars scanned 4 times (red dots in Figure 9) are considered successful detections. Therefore, radar detection probability is determined as follows:

$$P_{single} = \frac{n_d}{n_r} \tag{10}$$

where P_{single} is the radar detection probability, n_d is the number of detected radars and n_r is the total number of 2D Gaussian-distributed radars.

Detection probability shows the probability of the stealth UAV being detected by an unknown enemy radar during the penetration mission, directly influencing the aircraft's combat damage ratio. During the penetration mission, the UAV flies to within 100 km of the combat target and launches its payload. If it is locked by the radar, it will launch in advance. While the stealth UAV independently executes the penetration mission, being

detected without launching the mission payload is considered a mission failure. The success probability of a single mission execution can be determined by the detection probability. This paper treats each mission execution as an independent event. Therefore, the survival probability of UAVs is approximately

$$P = (1 - P_{single})^N \tag{11}$$

where P_{single} represents the probability of successfully completing a single mission, N represents the flight sorties and P represents the probability of the stealth UAV's survival.

Whether the stealth UAV has completed its mission should be considered since the ability of missiles to launch and destroy targets differs. In actual combat, air defense weapon systems are very complex. Probability calculations necessitate extensive experimentation with air defense systems, which is nearly impossible during preliminary design phases. This paper simplifies the calculation when considering the enemy air defense system, linking missile hit probability to launch distance. The UAV carries a single loitering ammunition with an effective range of 350 km, comparable in terms of mass and performance with the ALTIUS-600 M as the reference missile, and the hit probability is set to four levels: impossible, low probability, high probability and inevitable. The estimated hit probabilities are listed in Figure 10.

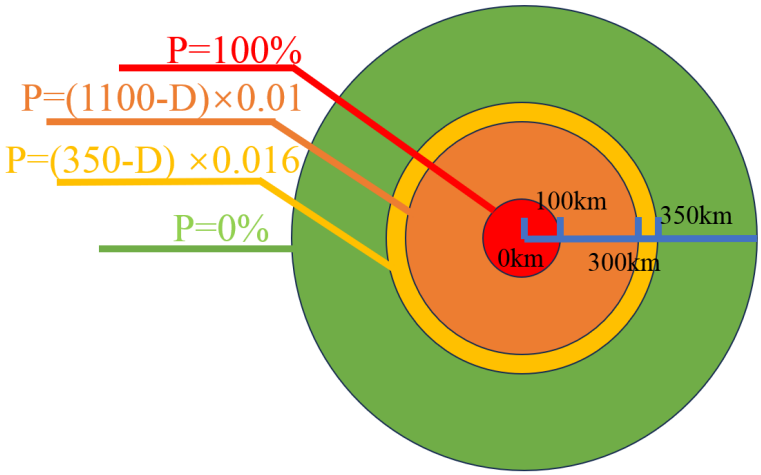


Figure 10. Hit probability diagram.

By calculating the average hit rate of each threat radar, the mathematical expectation for completing a single mission is transferred to the following:

$$P_{single} = \sum_{i=1}^{n} P_i \Big/ n \tag{12}$$

where n refers to the number of 2D Gaussian distributed radars and P_i refers to every hit probability encountering each radar under Gaussian distribution.

In probability statistics, events that occur very infrequently in a large number of repeated tests are referred to as low-probability events. Generally, two values ranging from 0.01 to 0.05 are used as criteria for low-probability events [28]. This paper considers 0.01 as the critical probability. Therefore, the following equation is derived between the maximum flight sorties and the radar detection probability:

$$P_{\max} = (1 - P_{single})^{N_{\max}} = 0.01 \tag{13}$$

where $N_{\max}$ represents the maximum flight sorties, and $P_{\max}$ represents the critical probability of the stealth UAV's survival.

Therefore, the average number of surviving flights is as follows:

$$N_{\max} = \log_{(1-P_{single})} 0.01 = \frac{\ln 0.01}{\ln\left(1 - P_{single}\right)} \tag{14}$$

For stealth UAVs performing penetration missions, the ratio of lift to drag L/D has a proportional relationship with the maximum combat radius derived from the Breguet formula:

$$Range = \left[\frac{V}{C} \ln \frac{m_0}{\left(m_0 - m_f\right)}\right] \cdot (L/D) \tag{15}$$

where $Range$ refers to the cruise range, V refers to the cruise velocity, C refers to specific fuel consumption, m_0 refers to the initial weight and m_f refers to the consumed weight.

The aircraft range is often used as a constraint when determining the overall parameters in the earliest stage of aircraft design. However, in actual combat, a longer cruise range often represents a bigger combat range that the aircraft can cover. Therefore, this paper defines E as the penetration efficiency coefficient, which represents the sum factor of the maximum cruise range for penetration missions throughout the entire life of the stealth UAV. The penetration efficiency coefficient serves as the optimization objective function:

$$E = N_{\max} \times (L/D) = \frac{(L/D)}{\ln\left(1 - P_{single}\right)} \ln 0.01 \tag{16}$$

2.3.2. Three-Dimensional Wing Optimization and Algorithm

Figure 11 shows the optimization flow chart. The orange box refers to radar detection probability model part and the green part refers to the conversion from radar detection probability to penetration efficiency.

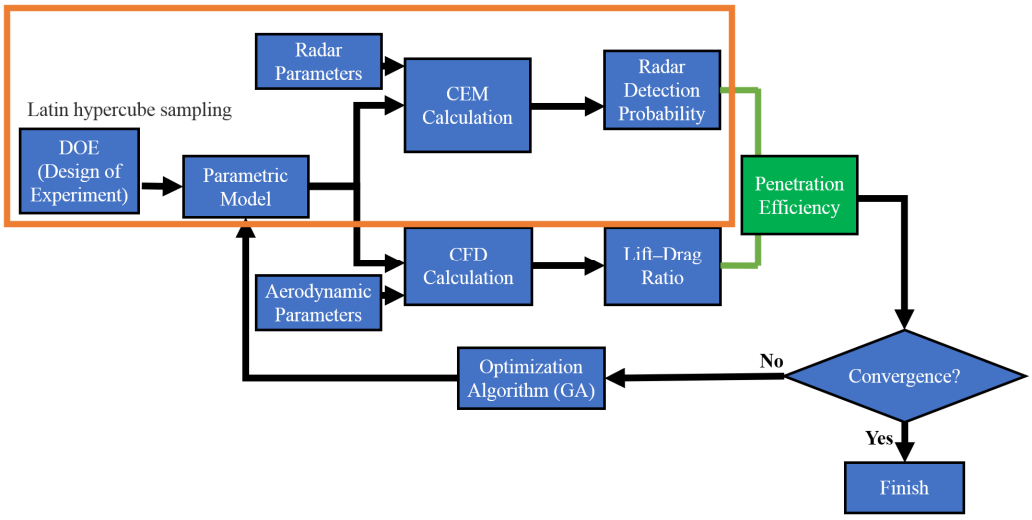


Figure 11. Flow chart of the aerodynamic/stealth optimization.

For the 3-D wing optimization, the wing sweep angle (χ), aspect ratio (A), wingtip twist angle (φ) and trailing edge turning point (b_1/b) are selected as design variables. These parameters can be combined to determine geometric properties such as wing span and chord length. The selected variables significantly influence the configuration of lambda wings. Numerical calculations involve discrete radar wave incident angles for RCS calculation. Therefore, the incident angles used in RCS calculations must include the wing sweep angle. Failure to do so would result in inaccurate RCS peak calculations. In

this paper, the wing sweep angle is adjusted in steps of 0.5 degrees, matching the RCS calculation increments.

The genetic algorithm [29] is an iterative, adaptive probabilistic search method based on the principle of natural selection and a genetic mechanism that simulates the developmental laws of biological evolution in nature. This algorithm is suitable for independent parametric variables within limited ranges and is tolerant of discontinuities in these variables. The genetic algorithm is adopted as the optimization technique, with Latin hypercube sampling used to generate the initial generation configuration. Table 3 outlines the boundaries of the parametric variables.

Table 3. Parametric variables.

Wing Variables	Baseline	Minimum	Maximum
Wing sweep angle/°	37	30	40
Wing aspect ratio	3.5	3	4.5
Wingtip twist angle/°	5	0	5
Trailing edge turning point/%	50%	30.0	55.0

3. Optimization Results and Discussion

After multiple genetic algorithm optimizations, the following results were obtained: Using the genetic algorithm over 160 generations, with 16 sample points per generation, a total of 2399 feasible results were obtained (93.7% feasibility rate). The optimization process is deemed converged as the optimal result remained unchanged during the last 300 iterations. Figure 12 and Table 4 present the results obtained from the genetic algorithm for aerodynamic/stealth optimization based on the radar detection probability model. As discussed in the preceding section, the evaluations of aerodynamic and stealth performance are integrated into penetration mission efficiency over the entire life cycle, shown in Figure 13.

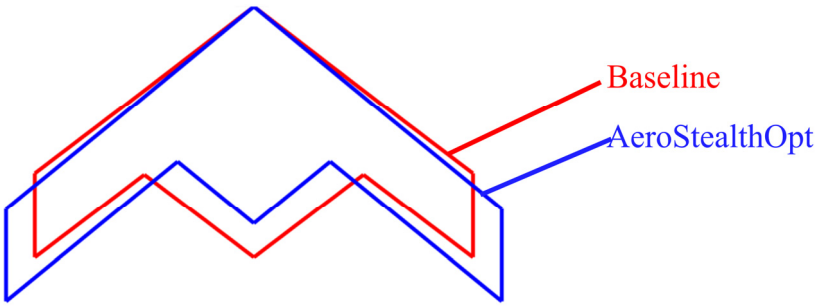


Figure 12. Geometry of baseline model and aerodynamic/stealth optimization model.

Table 4. Parameters of baseline model and aerodynamic/stealth optimization model.

Wing Variables	Baseline	AeroStealthOpt
Wing sweep angle/°	37	39
Wing aspect ratio	3.5	4.480
Wingtip twist angle/°	5	1.142
Trailing edge turning point/%	50%	30.79%
Radar detection probability	14.49%	14.24%
Maximum flight sorties	29.42	29.96
Lift–drag ratio	17.15	19.24
Penetration efficiency coefficient	504.54	576.38

These results indicate that the optimization trend tends towards increasing the aspect ratio and wing sweep angle. The twist angle and trailing edge turning point converge to

1.142° and 30.8%. The convergence process of the optimization is illustrated in Figure 13, showing that all four parametric variables converge within narrow ranges.

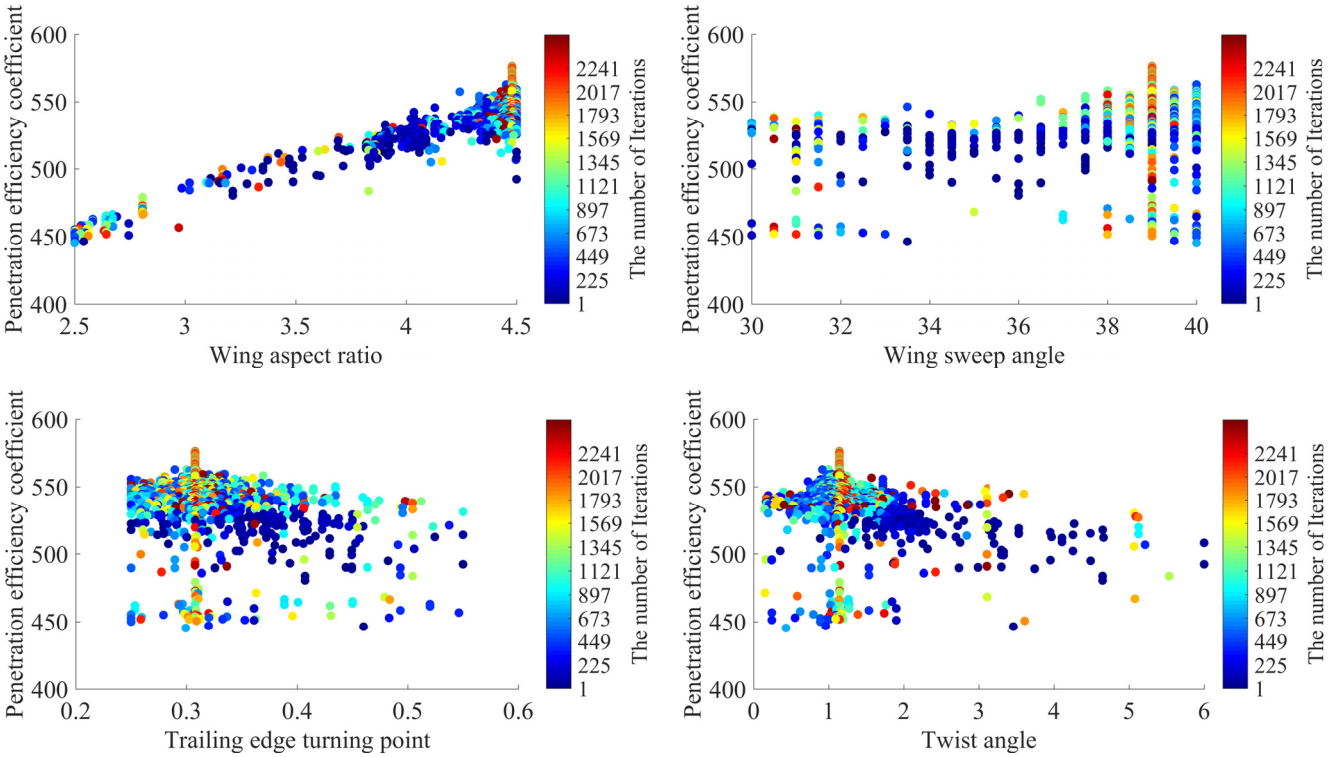


Figure 13. Parametric variables of feasible results and convergence histories.

The wing aspect ratio converges to 4.480, nearing its upper limit, which favors drag reduction. Figure 14 illustrates the relationship between the lift–drag ratio and wing aspect ratio, as well as the radar detection probability and wing aspect ratio. The wing aspect ratio emerges as a critical factor restricting aerodynamic performance, while its influence on stealth performance appears less pronounced.

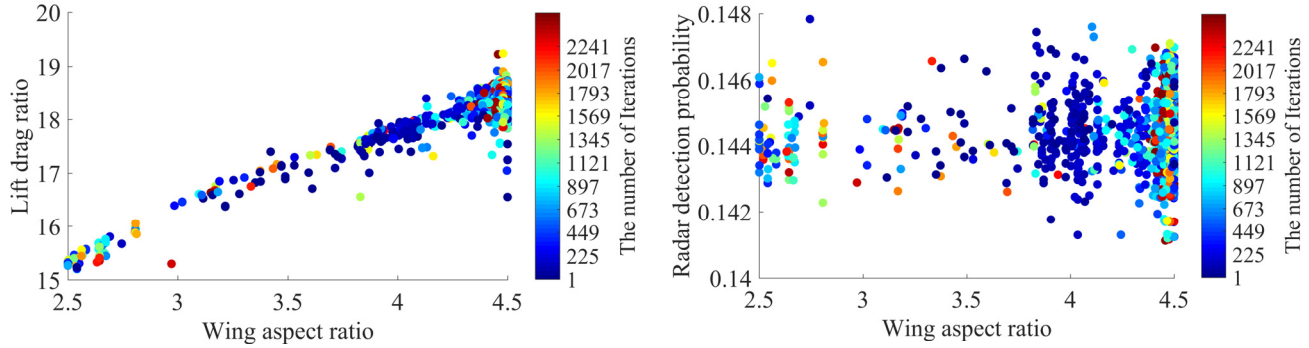


Figure 14. Wing aspect ratio convergence process.

The wing sweep angle converges to 39°, close to the upper boundary. Figure 15 shows that increasing the wing sweep angle enhances both aerodynamic and stealth performance during the initial stage of optimization. A larger wing sweep angle is beneficial for reducing subsonic drag and concentrating RCS peaks at larger incidence angles, making them more difficult to detect by radar, as shown in Figure 16. However, an excessive wing sweep angle can lead to decreased aerodynamic performance at low speed, which is the primary reason for imposing an upper bound for the wing sweep angle.

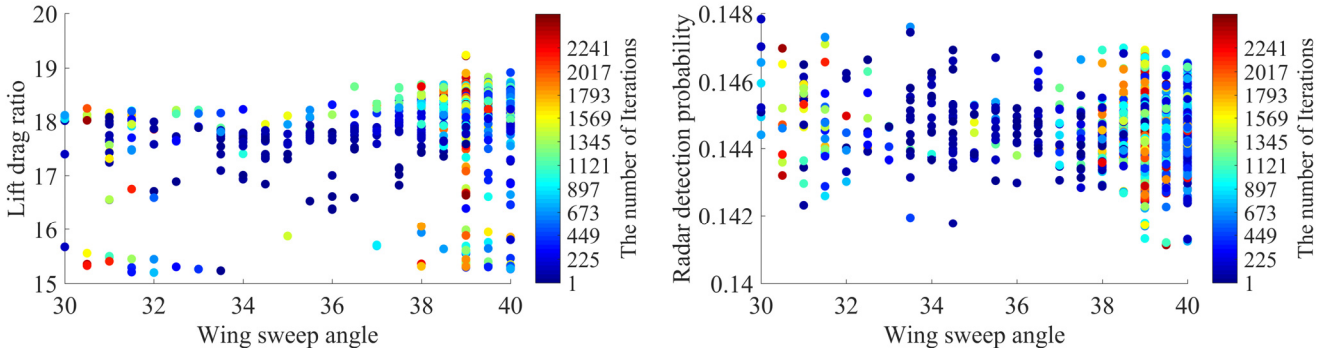


Figure 15. Wing sweep angle convergence process.

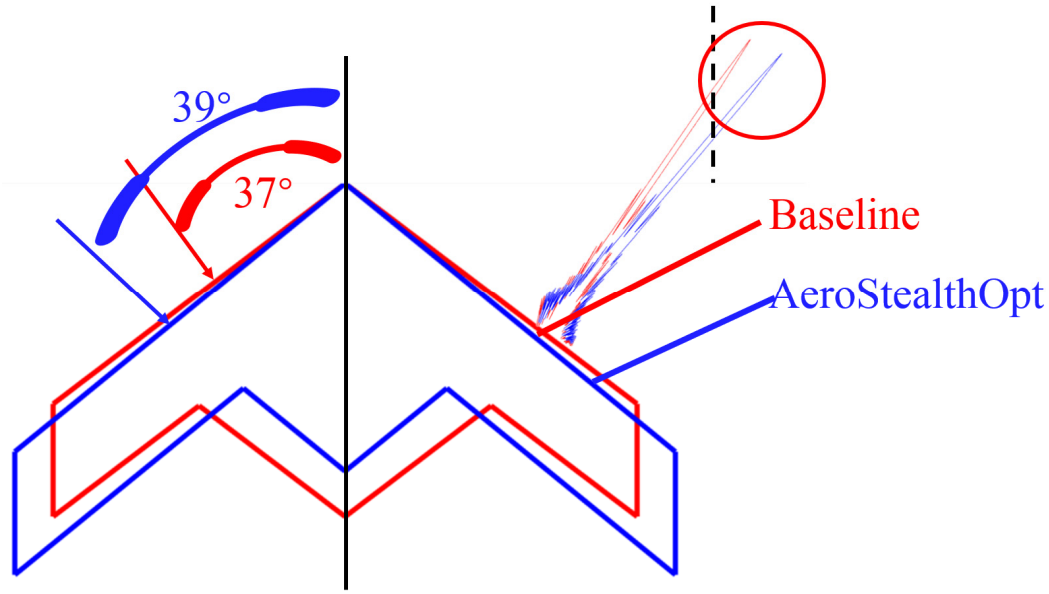


Figure 16. The relationship between wing sweep angle and RCS peak.

The trailing edge turning point is an important parameter that influences the ratio of inner and outer wing parts and the distribution of wing chord length. The optimization results show that the trailing edge turning point tends to move inwards towards the wing root as shown in Figure 17. Moving the trailing edge turning point inwards benefits both aerodynamic and stealth performance. A shorter chord length in the inner wing part aids in reducing drag and forward RCS. However, excessively inward movement of the trailing edge turning point increases in the thickness of the outer wing part, leading to higher drag. Regarding stealth performance, the radar detection model tends to decrease the maximum thickness of the lambda wing. The trailing edge turning point affects the distribution of chord length, thereby influencing the maximum thickness. The relationship is shown in Figure 18. Lambda-30, Lambda-40 and Lambda-50 denote the trailing edge turning points at 30%, 40% and 50%, respectively. The optimization trend is evident in Figure 17.

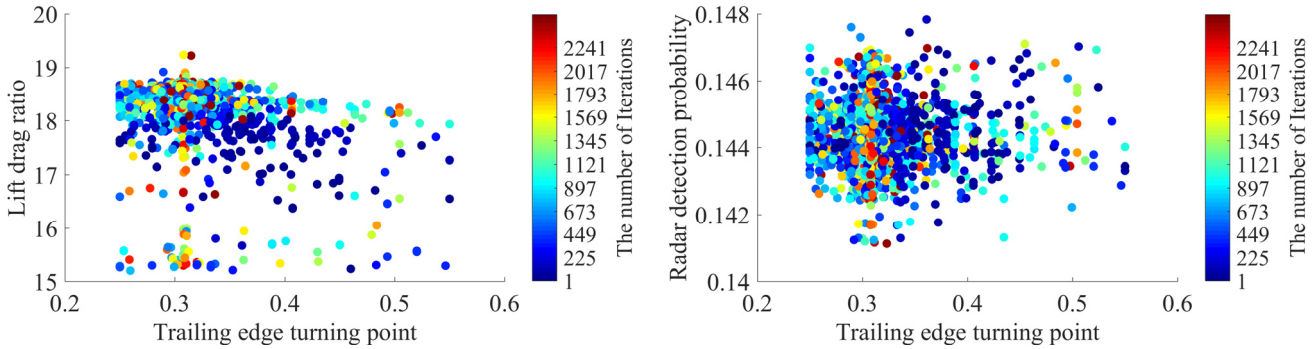


Figure 17. Trailing edge turning point convergence process.

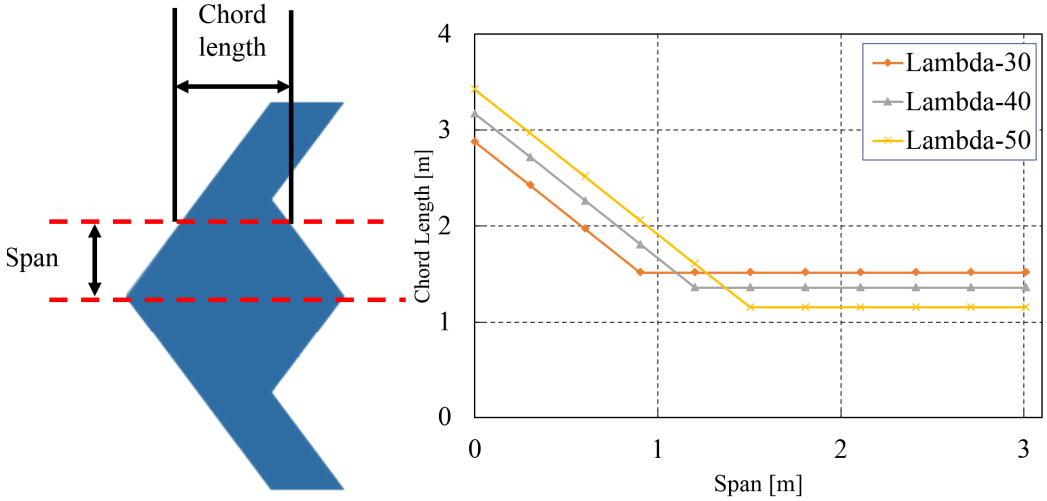


Figure 18. Relationship between trailing edge turning point and chord distribution.

Figure 19 shows the convergence relationship between the twist angle and lift–drag ratio and the relationship between the twist angle and radar detection probability. For stealth performance, the convergence relationship between the twist angle and radar detection probability is not obvious. However, reducing the twist angle is beneficial for reducing the cross-sectional area, which is slightly beneficial for stealth performance.

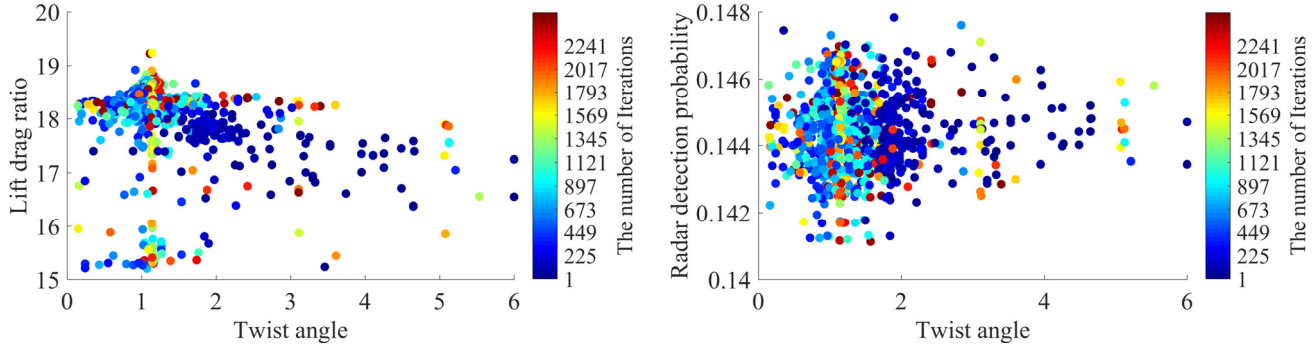


Figure 19. Twist angle convergence process.

Our results show that aerodynamic performance improvement has a large influence, while stealth performance improvement has a relatively minor influence. A Pearson correlation coefficient heatmap of the influence of the four parameters on the penetration efficiency coefficient is shown in Figure 20. The wing aspect ratio has a significant influence, the wing sweep angle has a moderate influence, and the trailing edge turning point and twist angle have minimal influence.

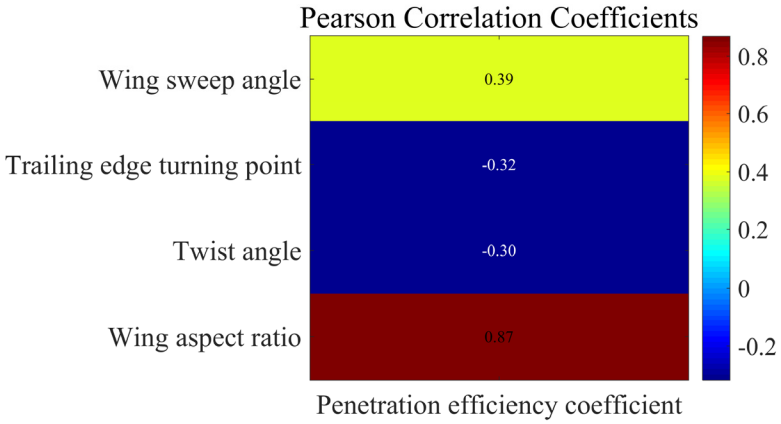


Figure 20. Pearson correlation coefficient plot.

From the results, we can see that the optimized configuration is closer to the upper limit of the wing sweep angle. A larger wing sweep angle disperses the RCS peak angle. This will increase the proportion of radars below the threshold, which is equivalent to increasing the proportion of blue dots in Figure 9. The influence of the wing sweep angle is moderate compared to the other four parameters. Upon increasing either the upper bound of the wing sweep angle or the radar scanning threshold, the proportion of blue dots will increase, and the wing sweep angle will have a stronger influence.

The wing aspect ratio reaches its upper limit. Due to limitations on wing area and airfoil, the cross-section of the leading edge remains unchanged. This is the primary reason for the minor RCS change except for the peak angle. If we include the airfoil as a parametric variable, the improvement in stealth performance will be greater.

The results show consistency between the convergence of the twist angle and aerodynamic performance. The reason is that the curvature variation near the leading edge of a blunt airfoil is continuous and the variation value is relatively low. Modifying the twist angle does not result in significant changes in stealth performance. If the leading edge is partially modified to a sharp profile, it will greatly increase the influence of the twist angle.

The influence of the trailing edge turning point on configuration and stealth is reflected in the distribution of reflection angle at the leading edge. Similar to the twist angle, the distribution of the reflection angle has a minor influence on stealth performance due to the blunt leading edge.

Different radar parameters will lead to various detection zones. Changing the parameters of the radar will result in doubling of the radar detection distance. If the SNR is increased from 30 dB to 40 dB, the radar detection distance will decrease by $(40\ \text{dB}/30\ \text{dB})^{1/4}$. This proportional relationship is consistent across other radar parameters, as shown in Figure 21. Figure 22 shows the radar distribution with an SNR of 40 dB. Increasing in SNR weakens radar detection capability, leading to fewer detected radars. Moreover, the proportion of radars falling below the scanning threshold increases. This emphasizes the importance of the incident angle of the RCS peak.

The scan filter threshold will affect the weight of the peak value and mean value on the detection probability. Excessive threshold values will make the incident angle of the RCS peak have no influence on detection probability. Conversely, too low a threshold will cause distortion in the detection probability model. For comparison, a radar distribution with a threshold set to 6 times is shown in Figure 23. It shows that most of the radars scanning from the RCS peak are filtered out. Excessive threshold values will lead to a low influence of the RCS peak during optimization.

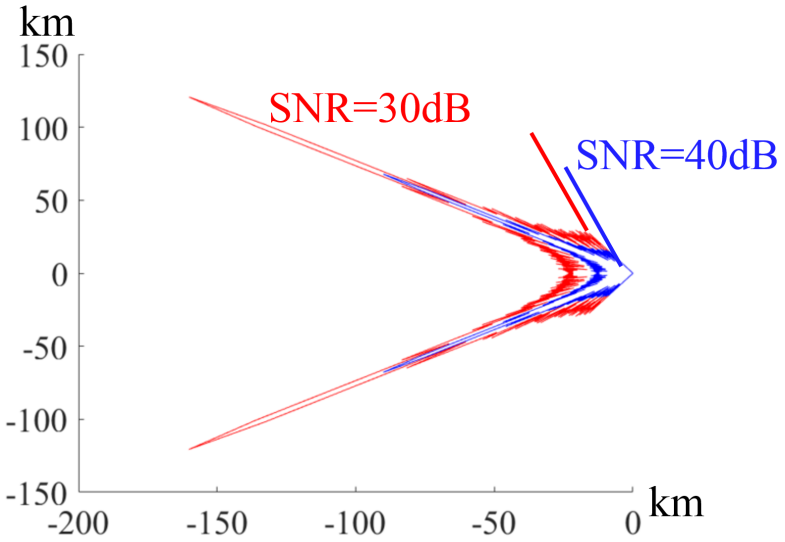


Figure 21. Radar detection distance relationship.

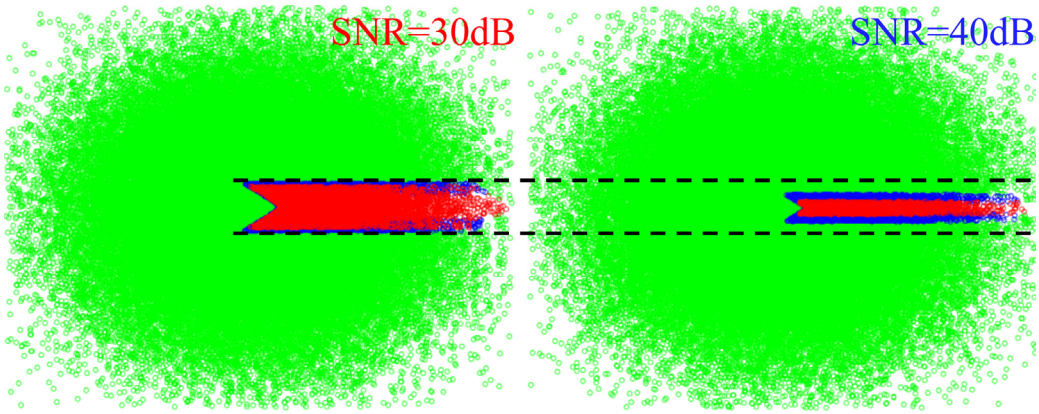


Figure 22. Radar distribution of different SNRs.

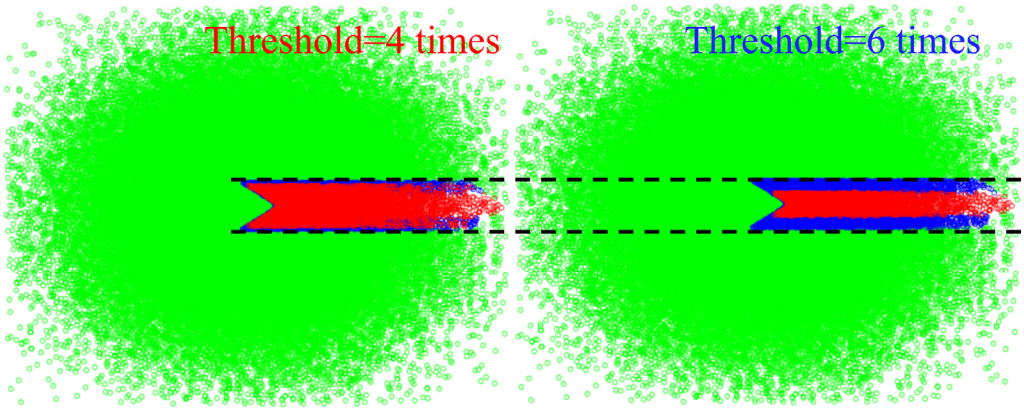


Figure 23. Radar distribution of different thresholds.

4. Conclusions

The proposed radar detection probability model solves the problem of balancing the relationship between the RCS peak and RCS mean values in traditional stealth optimization. Through this model, all incident angles are converted to detectable distance, and then converted to radar detection probabilities. This model naturally avoids the issue of peak

exposure being ignored and the problem of RCS peaks having an excessive influence on the radar detection distance.

The penetration efficiency model proposes a combination method of aerodynamic characteristics and stealth characteristics. This nonlinear combination method is different from the pareto front method or weighted average method. This model proposes penetration efficiency as the single optimization objective and makes the optimization process closer to a real penetration mission.

Following optimization, the penetration efficiency coefficient increases by 13.84% from the original baseline model. The result analysis shows improvements in both aerodynamic and stealth performance and indicates the feasibility of the optimization model. The analysis also indicates that the optimization tendency of stealth and aerodynamic has a strong correlation with the radar parameters.

Author Contributions: Conceptualization, methodology, software, validation, investigation and writing—original draft preparation, C.Y.; writing—review and editing, L.Z.; supervision and project administration, D.M. and Y.J. All authors have read and agreed to the published version of the manuscript.

Funding: This research received no external funding.

Data Availability Statement: The original contributions presented in the study are included in the article, further inquiries can be directed to the corresponding author.

Conflicts of Interest: The authors declare no conflicts of interest.

References

1. Ufimtsev, P.Y. Comments on diffraction principles and limitations of RCS reduction techniques. *Proc. IEEE* **1996**, *84*, 1830–1851. [CrossRef]
2. Zhou, L.; Huang, J.; Gao, Z.; Zhang, W. Three-Dimensional Aerodynamic/Stealth Optimization Based on Adjoint Sensitivity Analysis for Scattering Problem. *AIAA J.* **2020**, *58*, 2702–2715. [CrossRef]
3. Tianyuan, H.; Xiongqing, Y. Aerodynamic/Stealthy/Structural Multidisciplinary Design Optimization of Unmanned Combat Air Vehicle. *Chin. J. Aeronaut.* **2009**, *22*, 380–386. [CrossRef]
4. Pan, Y.; Huang, J.; Li, F.; Yan, C. Integrated design optimization of aerodynamic and stealthy performance for flying wing aircraft. In Proceedings of the International MultiConference of Engineers and Computer Scientists, Hong Kong, China, 15–17 March 2017; pp. 15–17.
5. Li, M.; Bai, J.; Li, L.; Meng, X.; Liu, Q.; Chen, B. A gradient-based aero-stealth optimization design method for flying wing aircraft. *Aerosp. Sci. Technol.* **2019**, *92*, 156–169. [CrossRef]
6. Li, M.; Chen, J.; Feng, X.; Qu, F.; Bai, J. An efficient adjoint method for the aero-stealth shape optimization design. *Aerosp. Sci. Technol.* **2021**, *118*, 107017. [CrossRef]
7. Wang, R.; Zhang, G.; Zhao, X.; Wang, B.; Ma, X. An Integrated Optimization Method of Wingtip Stealth/Aerodynamic Using Surrogate-Based Method. In Proceedings of the 2021 International Conference on Autonomous Unmanned Systems (ICAUS 2021), Changsha, China, 24–26 September 2021; Springer: Berlin/Heidelberg, Germany, 2021; pp. 348–357.
8. Taj, Z.U.D.; Bilal, A.; Awais, M.; Salamat, S.; Abbas, M.; Maqsood, A. Design exploration and optimization of aerodynamics and radar cross section for a fighter aircraft. *Aerosp. Sci. Technol.* **2023**, *133*, 108114. [CrossRef]
9. Zhou, Z.; Huang, J.; Yi, M. Comprehensive optimization of aerodynamic noise and radar stealth for helicopter rotor based on Pareto solution. *Aerosp. Sci. Technol.* **2018**, *82–83*, 607–619. [CrossRef]
10. Wu, D.; Long, T.; Li, Y.; Jiang, M.; Huang, B. Aero-structure-stealth coupled optimization for high aspect ratio wing using adaptive metamodeling method. In Proceedings of the 15th AI-AA/ISSMO Multidisciplinary Analysis and Optimization Conference, Atlanta, GA, USA, 16–20 June 2014; p. 2304.
11. Lu, X.; Huang, J.; Wu, Y.; Song, L. Influence of stealth aircraft dynamic RCS peak on radar detection probability. *Chin. J. Aeronaut.* **2023**, *36*, 137–145. [CrossRef]
12. Li, Y.; Wu, Z.; Huang, P.; Liu, Z. A New Method for Analyzing Integrated Stealth Ability of Penetration Aircraft. *Chin. J. Aeronaut.* **2010**, *23*, 187–193. [CrossRef]
13. Li, Y.; Huang, J.; Hong, S.; Wu, Z.; Liu, Z. A new assessment method for the comprehensive stealth performance of penetration aircrafts. *Aerosp. Sci. Technol.* **2011**, *15*, 511–518. [CrossRef]
14. Pachter, M.; Hebert, J. Minimizing Radar Exposure in Air Vehicle Path Planning. *IFAC Proc. Vol.* **2002**, *35*, 181–185. [CrossRef]
15. Luo, J.; Liang, Q.; Li, H. UAV penetration mission path planning based on improved holonic particle swarm optimization. *J. Syst. Eng. Electron.* **2023**, *34*, 197–213. [CrossRef]
16. Peng, Z.-H.; Sun, L.; Chen, J. Online path planning for UAV low-altitude penetration based on an improved differential evolution algorithm. *Chin. J. Eng.* **2012**, *34*, 96–101.

17. Zhu, W.; Duan, H. Chaotic predator–prey biogeography-based optimization approach for UCAV path planning. *Aerosp. Sci. Technol.* **2014**, *32*, 153–161. [CrossRef]
18. Xu, Q.; Ge, J.; Yang, T.; Sun, X. A trajectory design method for coupling aircraft radar cross-section characteristics. *Aerosp. Sci. Technol.* **2020**, *98*, 105653. [CrossRef]
19. Zhang, Z.; Jiang, J.; Wu, J.; Zhu, X. Efficient and optimal penetration path planning for stealth unmanned aerial vehicle using minimal radar cross-section tactics and modified A-Star algorithm. *ISA Trans.* **2023**, *134*, 42–57. [CrossRef] [PubMed]
20. Liu, D.; Xiong, J.; Wang, Y.; Huang, J.P. Research on Target Detection Probability Model of Penetration Plane During the Final Stage. In Proceedings of the 7th International Conference on Education, Management, Information and Mechanical Engineering (EMIM 2017), Shenyang, China, 28–30 April 2017; Atlantis Press: Amsterdam, The Netherlands, 2017; pp. 725–731.
21. Najafi, M.; Schmauss, B.; Schober, R. Intelligent reflecting surfaces for free space optical communication systems. *IEEE Trans. Commun.* **2021**, *69*, 6134–6151. [CrossRef]
22. Asvestas, J.S. The physical optics method in electromagnetic scattering. *J. Math. Phys.* **1980**, *21*, 290–299. [CrossRef]
23. Ergül, Ö.; Gürel, L. Benchmark solutions of large problems for evaluating accuracy and efficiency of electromagnetics solvers. In Proceedings of the 2011 IEEE International Symposium on Antennas and Propagation (APSURSI), Spokane, DC, USA, 3–8 July 2011; IEEE: New York, NY, USA, 2011; pp. 179–182.
24. Landry, N.; Goodrich, H.; Inacker, H.; Lavedan, L. Practical Aspects of Phase-Shifter and Driver Design for a Tactical Multifunction Phased-Array RADAR System. *IEEE Trans. Microw. Theory Tech.* **1974**, *22*, 617–625. [CrossRef]
25. Eliasson, P.; Peng, S.-H. Drag prediction for the DLR-F6 wing-body configuration using the EDGE solver. *J. Aircr.* **2008**, *45*, 837–847. [CrossRef]
26. Yuan, C.; Ma, D.; Jia, Y.; Yang, M.; Zhang, L. Numerical analysis of pitch-break and all moving wingtip aileron of lambda wing configuration. *Aerosp. Sci. Technol.* **2023**, *141*, 108508. [CrossRef]
27. Liu, X.; Wang, T.; Chen, J.; Wu, J. Efficient configuration calibration in airborne distributed radar systems. *IEEE Trans. Aerosp. Electron. Syst.* **2022**, *58*, 1799–1817. [CrossRef]
28. Burns, R.B.; Dobson, C.B. *Statistical Significance, Experimental Psychology: Research Methods and Statistics*; Springer: Dordrecht, The Netherlands, 1981; pp. 52–56.
29. Vose, M.D. *The Simple Genetic Algorithm: Foundations and Theory*; MIT Press: Cambridge, MA, USA, 1999.

Disclaimer/Publisher's Note: The statements, opinions and data contained in all publications are solely those of the individual author(s) and contributor(s) and not of MDPI and/or the editor(s). MDPI and/or the editor(s) disclaim responsibility for any injury to people or property resulting from any ideas, methods, instructions or products referred to in the content.